Report

Current Biology

Traction Forces Control Cell-Edge Dynamics and Mediate Distance Sensitivity during Cell Polarization

Highlights

- Traction forces correlate with the distance from the center to the edge of the cell
- Analysis of edge and stress dynamics suggests that stress triggers edge retraction
- Unlike traction stress, actin flow correlates with distance only during retraction
- Simple model reproduces force-distance relationship

Authors

Zeno Messi, Alicia Bornert, Franck Raynaud, Alexander B. Verkhovsky

Correspondence

zeno.messi@epfl.ch (Z.M.), alexander.verkhovsky@epfl.ch (A.B.V.)

In Brief

Messi et al. study traction force dynamics during cell polarization. The authors show that forces correlate with edge dynamics and the distance from the edge to the cell center, suggesting that traction stress organizes cell-edge activity by triggering transition from protrusion to retraction.

Messi et al., 2020, Current Biology *30*, 1762–1769
May 4, 2020
https://doi.org/10.1016/j.cub.2020.02.078

CellPress

CellPress

Current Biology
Report

Traction Forces Control Cell-Edge Dynamics and Mediate Distance Sensitivity during Cell Polarization

Zeno Messi,[1,4,5,*] Alicia Bornert,[1,3,4] Franck Raynaud,[2] and Alexander B. Verkhovsky[1,*]
[1]Laboratory of Physics of Living Matter, EPFL, Route de la Sorge, Lausanne 1015, Switzerland
[2]Scientific and Parallel Computing Group, Computer Science Department, University of Geneva, Route de Drize, Carouge 1227, Switzerland
[3]Present address: UMR S1255, Etablissement Français du Sang, rue Spielmann, Strasbourg 67000, France
[4]These authors contributed equally
[5]Lead Contact
*Correspondence: zeno.messi@epfl.ch (Z.M.), alexander.verkhovsky@epfl.ch (A.B.V.)
https://doi.org/10.1016/j.cub.2020.02.078

SUMMARY

Traction forces are generated by cellular actin-myosin system and transmitted to the environment through adhesions. They are believed to drive cell motion, shape changes, and extracellular matrix remodeling [1–3]. However, most of the traction force analysis has been performed on stationary cells, investigating forces at the level of individual focal adhesions or linking them to static cell parameters, such as area and edge curvature [4–10]. It is not well understood how traction forces are related to shape changes and motion, e.g., forces were reported to either increase or drop prior to cell retraction [11–15]. Here, we analyze the dynamics of traction forces during the protrusion-retraction cycle of polarizing fish epidermal keratocytes and find that forces fluctuate together with the cycle, increasing during protrusion and reaching maximum at the beginning of retraction. We relate force dynamics to the recently discovered phenomenological rule [16] that governs cell-edge behavior during keratocyte polarization: both traction forces and probability of switch from protrusion to retraction increase with the distance from the cell center. Diminishing forces with cell contractility inhibitor leads to decreased edge fluctuations and abnormal polarization, although externally applied force can induce protrusion-retraction switch. These results suggest that forces mediate distance sensitivity of the edge dynamics and organize cell-edge behavior, leading to spontaneous polarization. Actin flow rate did not exhibit the same distance dependence as traction stress, arguing against its role in organizing edge dynamics. Finally, using a simple model of actin-myosin network, we show that force-distance relationship might be an emergent feature of such networks.

RESULTS AND DISCUSSION

Stress Foci Localize to the Tips of Protrusions during Cell Polarization

Uncovering the mutual relationship between adhesion, traction forces, and cell shape is important to understand cell-shape changes and motion [11, 12, 14, 15, 17–24]. In a model system of migrating fish epidermal keratocytes, it is relatively well understood how actin assembly, adhesion, and contractile forces determine the regular shape of polarized cells [17, 18], but much less is known about what happens when the cells actively change their shape. In order to investigate traction force dynamics during keratocyte shape fluctuations and polarization, we plated cells on compliant polyacrylamide (PAA) substrates. In our recent study, we described how local protrusion-retraction fluctuations in fish epidermal keratocytes lead to overall cell polarization [16]. We uncovered a phenomenological rule that governs these dynamics: transitions from protrusion to retraction preferentially happen at a certain threshold distance from the cell center. This distance-sensing rule implemented in a stochastic model was sufficient to reproduce the emergence of polarized state and directional motion from apparently disorganized protrusion-retraction fluctuations. We tested whether the cells on PAA substrates exhibited the same behavior as we have previously observed on rigid glass substrates. On very soft PAA (3*KPa*), keratocytes initially spread to a much smaller area than on glass, exhibited only small shape fluctuations, and polarized very rapidly. However, increasing PAA elastic modulus to 16*KPa* yielded the behavior that was indistinguishable from the one observed on glass: cells spread and exhibited large protrusion-retraction fluctuations and apparent waves traveling around the cell perimeter, eventually consolidating in one protruding front and one retracting back (Figure 1A; Video S1). In order to have sufficiently large time and space window to observe polarization process, we have selected PAA with elastic modulus of 16*KPa* for all subsequent experiments.

Physical mechanism of how the cell controls the distribution of protrusion-retraction transitions is not known. Here, we investigate traction force dynamics during polarization to test the hypothesis that traction force could be the mediator of distance sensing and a trigger for protrusion-retraction switches. Traction force microscopy of polarizing cells revealed a very dynamic

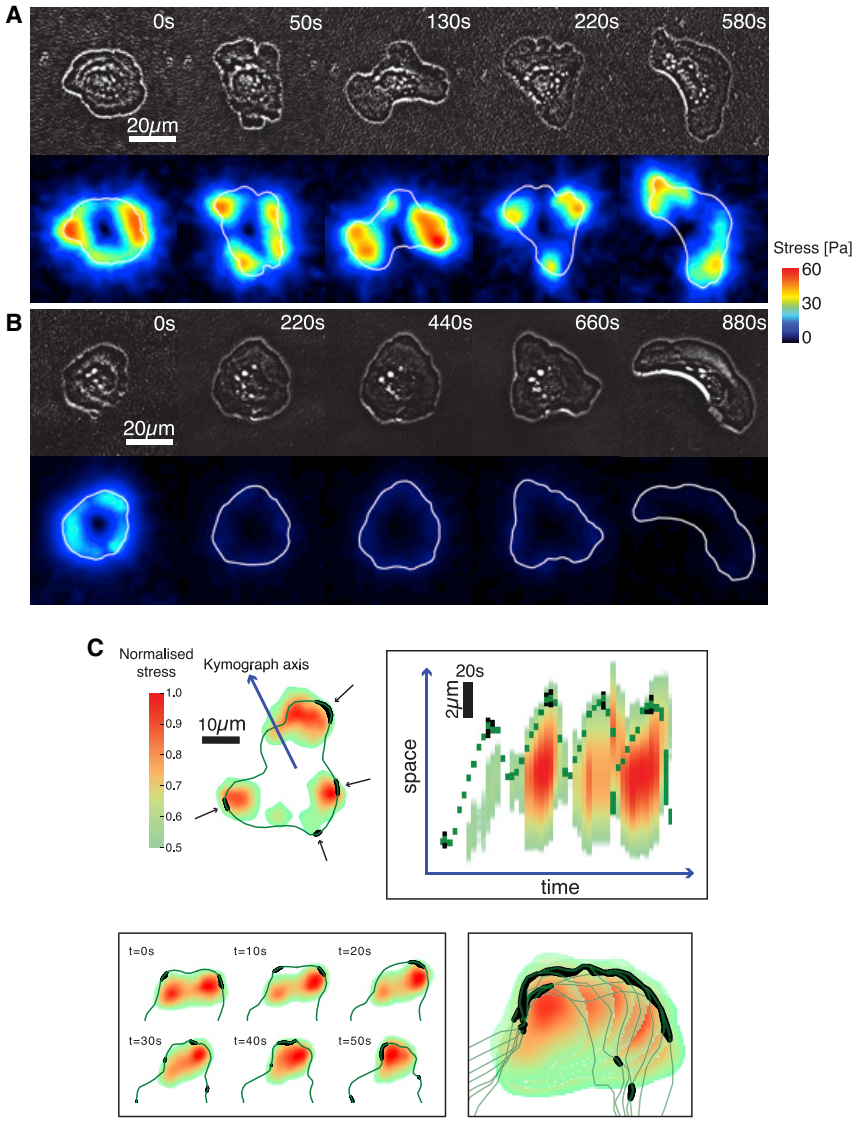

Figure 1. Stress Foci Localize to the Tips of Protrusions near the Areas of Protrusion-Retraction Switches

(A and B) Phase contrast (top rows) and corresponding traction stress (bottom rows) images from sequences of polarizing cells. Phase contrast images are sharpened to make cell outline clearly visible on the background of substrate with beads. Stress is color coded, and the cell outline is shown in white in traction stress images. Scale bars, 20 μm; time is indicated in seconds. Shown in (A) is polarization in control conditions. Shown in (B) is polarization in the presence of 100 μm (−)-blebbistatin.

(C) Outlines (dark green) of polarizing cells with protrusion-retraction switches (black) and color-coded traction stress. Stress is normalized by the maximal stress in the sequence. On top, one frame from the sequence (left) and kymograph (right) along the axis that is shown with the blue arrow on the left. Kymograph corresponds to the part of the sequence before polarization. Scale bars, horizontal 20s, vertical 2 μm. On the bottom, a detail of the outline is shown; six consecutive frames shown at the left are superimposed in one image on the right.

See also Figure S1 and Videos S1–S4.

stress distribution (Figure 1A; Video S1). At all stages of polarization, traction forces were oriented generally radially toward the cell center. At the onset of spreading, the region of high stress formed an almost continuous ring at the cell periphery, but then the ring broke in the multiple foci, which moved, appeared, disappeared, fused, and split but generally always followed the tips of extending regions of the cell. When the cells eventually polarized and started to move persistently, stress foci localized to the two lateral cell extremities (Figure 1A) (580s), as previously reported [25, 26]. Thus, both during and after polarization, stresses were found in the regions of the cell that were most distant from the cell center.

Visualizing force foci simultaneously with the regions of protrusion-retraction switches (defined in the substrate frame as described in [16]; see also STAR Methods) in the video sequences revealed a close proximity and a coordinated movement of switch sites and force foci (Figure 1C; Video S2). Note that protrusion-retraction switches mapped directly to the cells edge, although the centers of the force foci localized inside the cell perimeter at a small distance from the edge, so there was no direct colocalization between the two. Nevertheless, proximity between the switches and force foci was apparent visually and also revealed by plotting the distribution of their separating distances. This distribution peaked at 5 μm, which is comparable to the width of the lamellipodia, suggesting that force foci were localized at focal adhesions at its base (Figure S1A). More evidence for the coordination between edge dynamics and the stress emerged from the comparison of the time evolutions of edge position and stress along the same radial line (Figure 1C, kymograph). In multiple cycles of protrusion and retraction, force spot followed the edge, moving outward and increasing in intensity during protrusion and shifting inward and diminishing during retraction. Taken together, these observations are consistent with the idea that the increase of inward-oriented traction forces during protrusion leads to eventual switch to retraction, which might be powered by the same forces.

Treatment of the cells with contractility inhibitor blebbistatin prior to polarization dramatically reduced not only traction forces but also the dynamics. Treated cells exhibited only very small protrusion-retraction fluctuations (Figure 1B). They eventually started to move but did not keep a stable crescent shape, instead either extending uncontrollably in width or splitting into fragments (Video S3). Such behavior was observed in other cell types and also predicted theoretically [27, 28]. It points to the importance of the traction forces to the ability of the cell to control their size and to retract its edge properly. Finally, application of the external force on a blebbistatin-treated cell by pulling on the compliant substrate with a micropipette induced dramatic

edge retraction and eventual polarization (Video S4). These observations suggest together a possible causal relationship between traction stress and edge retraction.

Traction Forces Increase with Distance from the Cell Center and in Time during Protrusion and Shortly after the Onset of Retraction

In our recent study, we have established that protrusion-retraction switches happen preferentially at the longest distance from the geometrical cell center. If these switches are indeed triggered by the increase in traction force, one should expect that traction forces increase with the distance from the cell center. We have plotted local stresses within the cell area versus distances from the cell center to the locations where these stresses were measured (see STAR Methods). Figure 2A demonstrates a strong positive correlation between the normalized stress and the normalized distance (Spearman's rank correlation coefficient $\rho_S = 0.67$). Normalization allowed aggregating the data from long sequences of multiple cells. Non-normalized stress-distance relationships revealed that maximal center-to-edge distance tended to increase with time during polarization process, although the local stress tended to decrease. Nevertheless, positive correlation between the non-normalized values of stress and distance was always evident when considering relatively short time intervals, including parts of the sequences after polarization, when the stress foci localized to lateral cell extremities (Figure S2B).

To get more insight into force-distance relationship, we compared maximal center-to-edge distances and stresses in the cells under different conditions: on substrates of various rigidities and under the influence of drugs modifying myosin contractility and actin polymerization (Figure 2B). As the majority of protrusion-retraction switches happen at the maximal distances from the center to the edge, the maximal center-to-edge distance is a measure of switching distance. On soft substrates, the cells exhibited lower maximal extensions and lower traction stresses than on rigid substrates. This is consistent with previous findings about adhesion reinforcement by substrate rigidity [20, 21]. Contractility activator calyculin A and low doses of actin polymerization inhibitor cytochalasin D both induced cells to retract, which was accompanied by a decrease in traction stress. As already mentioned, inhibitor of myosin activity blebbistatin induced dramatic decrease in traction stress. This was accompanied by a change in the distribution of maximal cell extension: the cells generally extended and fluctuated less than in control before polarization but extended much more once polarized. This is reflected in the asymmetric extension distribution with large number of very high extension values (Figure 2B). These results suggest that cell extension and traction stresses are controlled by multiple factors involving the balance of adhesion strength, actin protrusion, and contractility. For example, decrease in cell extension and traction stress in the presence of calyculin could be explained by increase of contractility without matching increase in adhesion so that enhanced cytoskeletal contraction led to retraction but did not result in increased traction at the substrate level. Importantly, in all conditions except blebbistatin treatment, the changes in cell extension were matched by parallel changes in traction stresses. Thus, under different conditions, cells retracted at different distances and at different stress values, but the stress-distance relationship was largely preserved through variety of conditions.

Correlation between maximal stress and the longest cell dimension was previously reported in a study using stationary cells and patterned substrates to allow precise control over the cell shape [5]. Another study employing cell shape patterning suggested that the overall magnitude of the traction forces depends on the cell spread area, although their local values are defined by the curvature of the cell edge [6]. However, in polarizing keratocytes, we did not observe a correlation between the stress and local edge curvature (Figure S2A) ($\rho_S = 0.11$). Interestingly, the behavior of protrusion-retraction switches in this respect paralleled the behavior of stress: switches were enriched at high distances from the cell center, but not enriched at high edge curvature (Figure S1B).

To get more insight into the relationship between traction stress and edge dynamics, we investigated how stress and cell edge position changed with time. Because we were specifically interested in protrusion-retraction events, we identified many such events and measured the stress and edge velocity around the time of these events (see STAR Methods). At the onset of protrusion, stress was low and protrusion rate was high. With the extent of protrusion, its rate gradually decreased while the stress increased continuously during protrusion and also for a few seconds after the onset of retraction, decreasing rapidly thereafter (Figure 2C). Interestingly, the maximum of retraction velocity was also observed shortly after the onset of retraction, coinciding in time with the stress maximum. This coincidence might indicate that the origin of this high stress was viscous friction between retracting cell structures and the extracellular matrix [29]. Complementary analysis of the relationship between stress and edge dynamics is provided by measuring the correlation between the change of stress and the edge velocity. Change of stress was measured between two consecutive frames. Velocity was determined from the change of edge position between two frames. We measured the time correlation function of stress and velocity, i.e., how the correlation between the change of stress and edge velocity depended on the time interval between the two measurements (see STAR Methods). The highest correlation was observed when the velocity measurement was shifted between 10 and 20*s* backward with respect to the stress measurement (Figure 2D). In other words, when the stress increased, the velocity was most likely to be positive (protrusion) a few seconds before, and if the stress decreased, the velocity was most likely to be negative (retraction) a few seconds before. This finding reinforces the previous result that stress increases during protrusion and for a short time after the retraction onset.

This analysis is consistent with a previous study where force dynamics during the protrusion-retraction cycles in fibroblasts was deduced from the patterns of actin flow [13] but is at odds with the idea that retraction is triggered by weakening of the adhesions at the cell edge [15]. If this were the case, one would expect the traction stress to decrease prior to the onset of retraction. In contrast, we observed that the stress still increased in the beginning of the retraction phase, suggesting that the adhesions persisted and continued to transmit force. Later in the retraction phase, we have observed that the stress does decrease, suggesting that the adhesions are eventually released. This is consistent with the observations of [15]; however, this is not

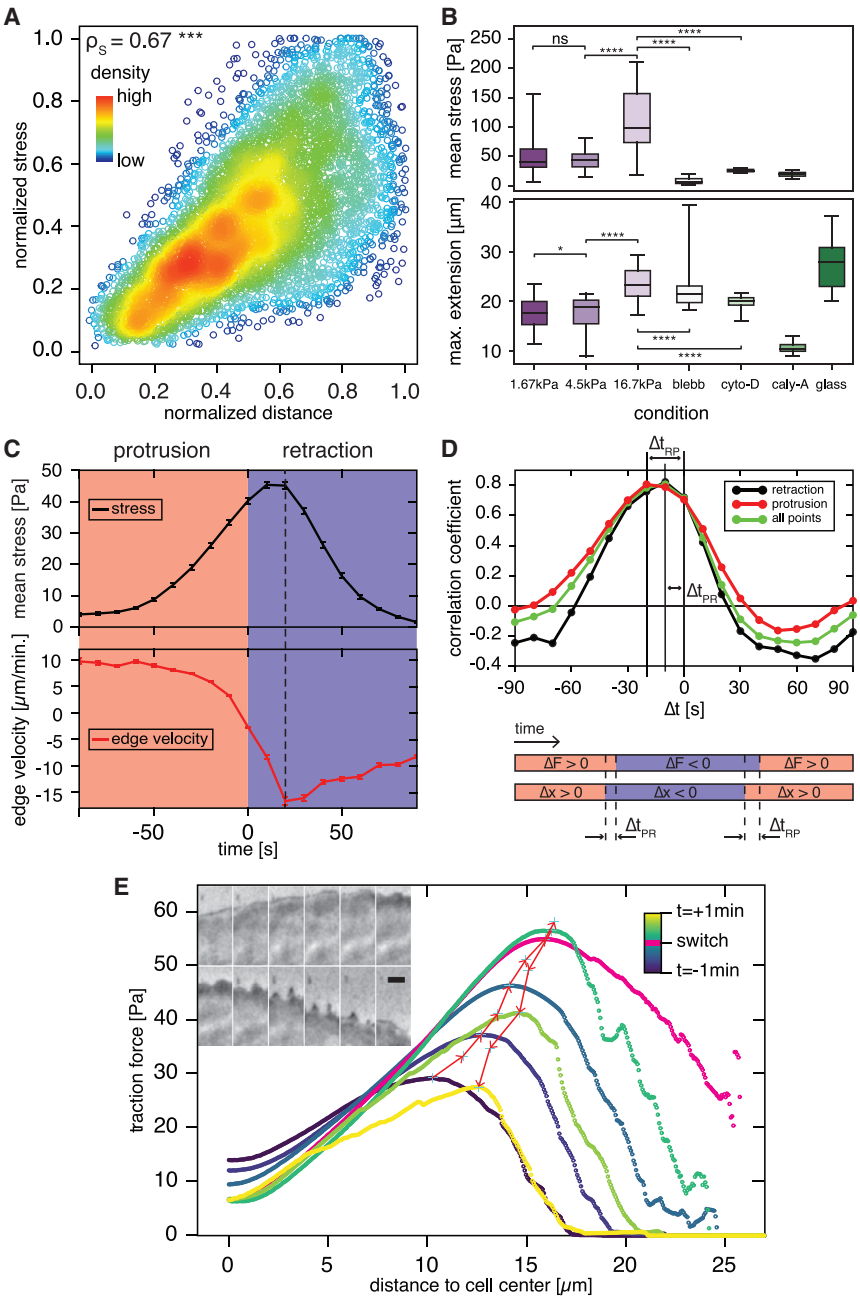

Figure 2. Traction Stress Increases with Distance from Cell Center and Correlates Spatially and Temporally with Edge Dynamics

(A) Plot of normalized stress versus normalized distance to the cell center. Data are aggregated from 306 frames of traction force microscopy sequences from 3 different cells; for clarity, 3% of the data points are displayed. Stress and distance are normalized in each frame by their maximal absolute values in the frame. Color codes for the density of data points are shown. Value of Spearman's rank correlation coefficient (ρ_S) is indicated, p value $p < 10^{-3}$.

(B) Distribution of the maximal extension of the edge and mean stress in the cell for different experimental conditions. 1.67 kPa, 4.5 kPa, 16.7 kPa, and *glass* denote different substrate rigidities. Measurements in the presence of 100 μM blebbistatin, 200 nM cytochalasin D, or 25 nM calyculin A were all performed on 16.7-kPa gel and are labeled as *blebb*, *cyto-D*, and *caly-A*, respectively. Boxes extend between the first and third quartiles. The bar in the box is the mean. The whiskers extend between the 5th and 95th percentiles. "*" denote the p value of a Mann-Whitney test. *$p < 10^{-1}$ and ****$p < 10^{-4}$.

(C) Time evolution of mean stress (top) and mean radial edge velocity (bottom) during multiple protrusion-retraction events ($n = 878$ events). Time is set to 0 at the onset of retraction. Edge velocity is defined as positive during protrusion. Dashed line indicates maximal retraction speed. Light red and blue background colors indicate, respectively, protrusion and retraction.

(D) Top: correlation between local edge velocity and local variation of stress. Green curve shows correlation coefficient from all data points and red and black curves from the points in protrusion only and retraction only, respectively. Highest correlation is observed when the stress measurement is shifted by −10 to −20s with respect to the velocity measurement. On the bottom, a diagram illustrating the time shift is shown. Light red and blue colors represent the positive and negative velocity (Δx) and change of stress (ΔF); Δt_{PR} is the likeliest delay between the onset of retraction and the time at which the stress starts to decrease, and Δt_{RP} is the likeliest delay between the onset of protrusion and the time when the stress begins to increase.

(E) Mean radial stress-distance profiles during protrusion-retraction cycles. The profile corresponding to the first frame in retraction is shown in pink. Red arrows indicate stress maxima in each profile. Time intervals between consecutive profiles are 20s. In the inset, interference reflection microscopy of a cell region undergoing protrusion-retraction event is shown. Scale bar, 2 μm; time interval between frames 6s.

See also Figure S2 and Video S5.

what triggered the onset of retraction. Importantly, unlike what was reported in [15], we have only very rarely observed that the cells maintained regular discoid shape prior to polarization and then polarized by means of a single retraction at the prospective rear; in contrast, majority of the cells exhibited large protrusion-retraction fluctuations, which did not result immediately in polarization. Polarization by a single retraction was more often observed on low rigidity gel or in the presence of blebbistatin. The differences in stress dynamics between our work and [15] could be related to these differences in morphology. The reason for it is unknown; it is possible that a subtle shift in balance between contractility and adhesion strength affects polarization pathway.

We have subsequently analyzed how the position of the stress foci changes with the edge position. Plots of the stress profiles in the radial sectors from the cell center to the edge at different times with respect to protrusion-retraction switch (Figure 2E) showed that the position of stress maximum followed the cell

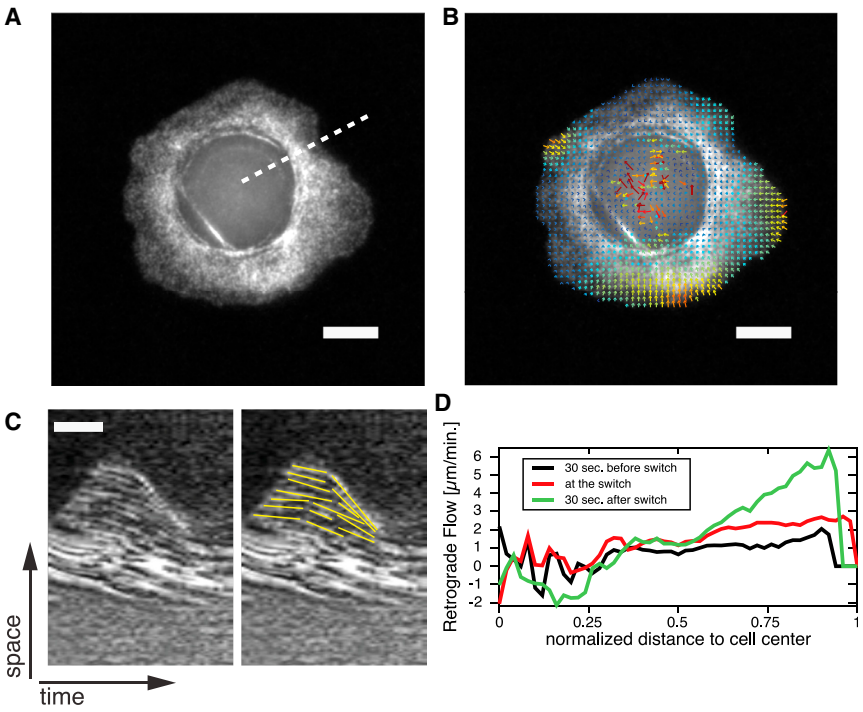

Figure 3. Actin Flow Rate Increases with Distance during Retraction but Is Constant during Protrusion

(A) Fluorescent speckle microscopy image of a polarizing cell injected with Alexa-phalloidin.

(B) Flow velocity map superimposed on the image.

(C) Kymograph along the dashed line in (A). Actin speckle trajectories are marked in yellow in the image on the right to highlight the flow. Scale bar, 2 μm and 50s.

(D) Mean actin flow velocity versus distance to the cell center at different times relative to the time of the switch from protrusion to retraction. The data are aggregated from 40 velocity maps.

Scale bars, 20 μm in (A and B).

edge: stress maximum shifted outward during protrusion and inward during retraction. This behavior could be explained by the assembly of new adhesions during the edge advance and sliding of adhesions during its retreat. Consistent with this idea, interference reflection microscopy demonstrated gray areas of cell close contact with the substrate expanding during protrusion and subsequently concentrating into dark foci and sliding back during retraction (Figure 2E, inset; Video S5). Note that, in persistently migrating keratocytes, largest adhesions that coincide with highest traction stress at the flanks of the cell [25, 30] were found to slide during cell motion [26, 31]. Lateral flanks of migrating cells are analogous to the tips of protruding segments in fluctuating cells in a sense that both are the sites where the majority of transitions from protrusion to retraction are observed [16]. The similarity of the edge, force, and adhesion behavior in fluctuating and migrating cells is consistent with the idea that local cell-edge dynamics follows the same rules throughout the process of polarization [16]. Our analysis thus suggests that, both in polarizing and migrating cells, increase of traction force causes adhesions to slide and eventually to detach. Sliding of adhesions likely destabilizes the surrounding actin network, including its parts distal from the adhesion, causing network collapse and the retraction of the whole edge. The fact that adhesions continue to transmit force at the onset of sliding is potentially significant because it means that the actin network remains under tension, facilitating building and stabilization of cytoskeletal structures, such as transverse actin arcs [22, 23]. This might also promote formation of highly curved plasma membrane sites contributing to re-initiation of protrusion [32]. The traction-force-induced retraction might not be the only possible mechanism. For example, in blebbistatin-treated cells, edge retraction is likely caused by membrane tension [26, 33]. However, elongation and fragmentation of the cells in the presence of blebbistatin suggests that traction forces are necessary to confer distance sensitivity to retraction process, helping the cell to keep integrity and stable shape.

Actin Flow Does Not Follow the Same Dynamics as the Traction Force

Next, we tested whether actin flow is responsible for the increase of the traction stress with the distance from the cell center. Previously, the onset of retraction in polarizing cells was associated with the increase in the rate of actin retrograde flow [34]. If actin flow is driven by contraction of multiple actin-myosin units connected in series, one could expect that the flow velocity at the extremities of the contractile segment would increase with the overall length of the segment, i.e., with the cell center-to-edge distance. Traction forces could be generated because of a viscous-like friction at the adhesions at the termini of contractile chains. In this case, the traction force dynamics at the adhesions might parallel the dynamics of actin flow and, similar to actin flow, feature a distance-dependent increase. To test these ideas, we have analyzed actin flow patterns in polarizing cells injected with Alexa-phalloidin (Figure 3). Kymographs of actin flow demonstrated that, consistent with previous reports, flow velocity increased upon the onset of retraction (Figures 3A and 3B). However, flow velocity appeared constant in time and independent of the distance throughout the protrusion phase. Kymographs only present the dynamics along individual selected directions. We have also generated flow velocity maps over the whole cell by using particle image velocimetry (Figure 3C; see STAR Methods). Average center-to-edge flow velocity profiles were plotted for the time points in protrusion, retraction, and at the protrusion-retraction switch (Figure 3D). Profiles in retraction featured high flow rate and a prominent increase with the distance from the cell center consistent with a telescopic contraction of multiple units connected in series. However, the profiles shortly before the onset of retraction and at the moment of the switch featured nearly constant flow velocity independent of the distance from the cell center. Thus, actin flow dynamics cannot account for the major features of the stress pattern, namely for the increase of stress during protrusion and its distance dependence.

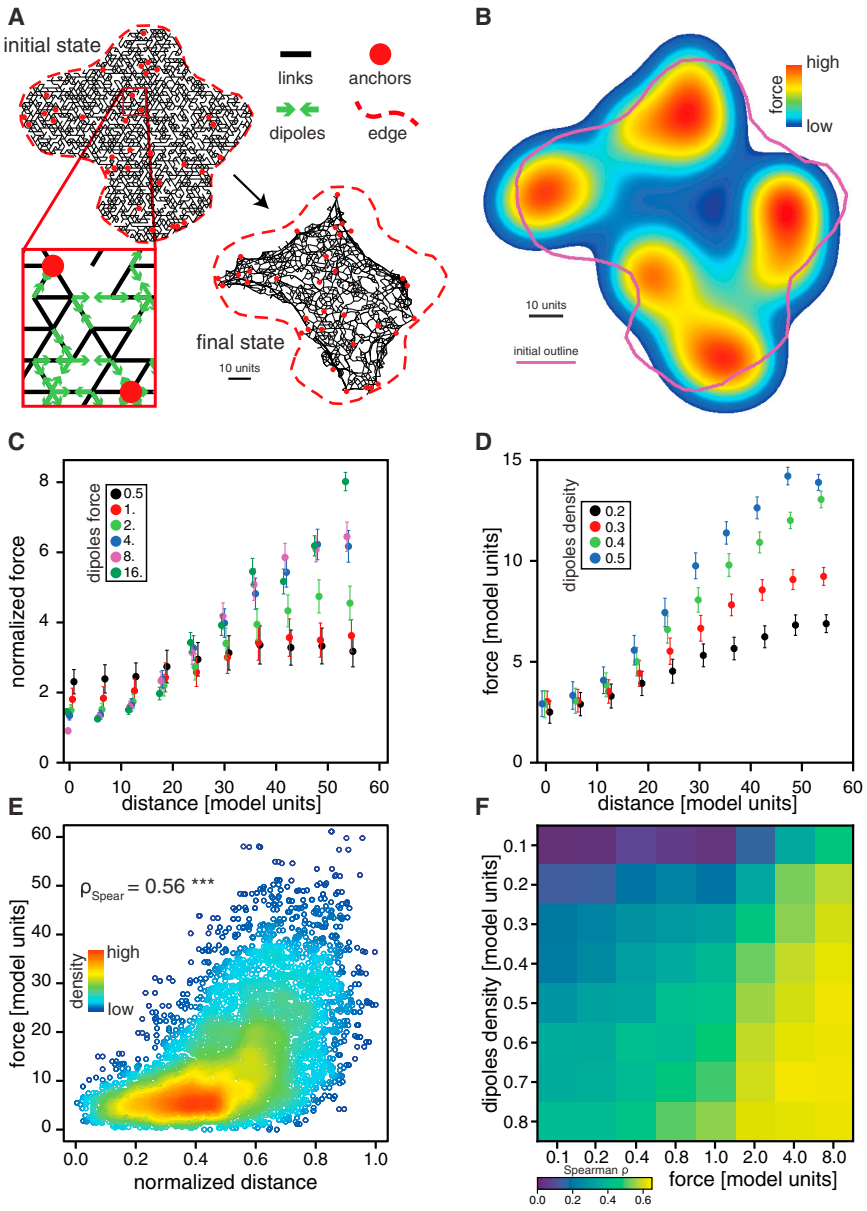

Figure 4. Simple Model of Actin-Myosin Network Reproduces Force-Distance Relationship

(A) Initial and final state of a typical simulation; black lines represent filaments and red circles the anchor points. Force dipoles (green arrows) are shown in a zoomed portion of the network (inset). Dashed red line is the initial outline of the system. Scale bar is 10 model-length units (5 times the length of a network hinge).

(B) Reconstituted force map; pink line shows the initial system outline. To create force map, the system final state was mapped to a 2,048 by 2,048 pixel image with pixel values corresponding to the force magnitudes at anchor points, and the image was blurred and color coded (color scale is logarithmic). Parameters are network density $\rho = 0.6$, dipole density $\rho_d = 0.3$, anchors density $\rho_a = 0.02$, links spring constant $\mu = 512$, and magnitude of the dipole force $M = 4$. Scale bar is 10 model-length units (5 times the length of a network hinge).

(C and D) Mean force at the anchors versus distance from the system centroid for different parameter values. Each data point is the average from 44 simulations (4 simulations made on each of 11 different initial outlines taken from experimental images). Parameters are network density $\rho = 0.6$, anchors density $\rho_a = 0.02$, and links spring constant $\mu = 256$.

(C) Dipole density is fixed at $\rho_d = 0.3$, and the dipole force is varied. Force is normalized by the magnitude of the force of one dipole M.

(D) Magnitude of the dipole force is fixed at $M = 2$, and the dipole density is varied.

(E) Density plot of the force distance relationship (parameters $\rho = 0.7$, $\rho_d = 0.3$, $\rho_a = 0.02$, $\mu = 256$, and $M = 4$) for 11 different initial outlines (8 realizations for each outline). Distance to the system centroid after minimization was normalized by the maximal distance in each realization. Each data point corresponds to the force measured on a single anchor. Spearman rank correlation coefficient $\rho_{Spearman} = 0.56$, p value $p < 10^{-3}$.

(F) Mean Spearman rank correlation coefficient for force-distance relationships for different values of the parameters ρ_d and M. Other parameters are $\rho = 0.6$, $\rho_a = 0.02$, and $\mu = 512$. At least 10 realizations on one initial outline were averaged for each set of parameters.

See also Table S1.

Simple Elastic Model of Actin-Myosin Network Reproduces Force-Distance Relationship

The observation that stress distribution was partially unrelated to the patterns of actin flow prompted us to investigate whether the features of stress, in particular its distance dependence, could be understood independently of actin dynamics, in terms of a simple elastic model of essentially static actin-myosin network. We simulated a simple elastic actin-myosin network following the ideas of Ronceray et al. [35]. Briefly, we generated filament network featuring asymmetric elasticity (spring constant for extension significantly higher than for bending compression) with attractive force dipoles inserted randomly between the nodes of the network (Figure 4A). Two important modifications were made with respect to [35]: first, the network was generated within the shapes taken from the experimental sequences of polarizing cells and, second, we released the constraint on the distribution of anchor points (emulating adhesions), placing them randomly in the bulk instead of just at the periphery. This was done with the idea to test whether traction force patterns could be reproduced in a model with minimal constraints on adhesions distribution. The network was allowed to deform to minimize the elastic energy, and the forces at the anchor points were computed and plotted versus distance of the anchor points from the geometrical center of the area (see STAR Methods).

Remarkably, the deformed network featured some alignment of filaments and dipoles into what could be considered rudimentary actin-myosin bundles and the force distribution recapitulated the experimentally observed trends (Figure 4A, final state). Similar to

experimental stress maps, simulated force maps displayed clusters of elevated forces at the periphery of the contour (Figure 4B). As in the experiments, forces increased with the distance from the contour center (Figure 4E). These trends were observed robustly for different contour shapes and for a range of simulation parameters (Figures 4C, 4D, and 4F). In particular, increase of force with distance was observed for different force dipole densities, and the slope of the relationship increased with dipole density. Intuitively, force-distance relationship in the model could be explained by screening of the internal anchors from forces by the bulk of the network and by other anchors, although most external anchors bear the major part of the force load. In the cytoskeleton, the distribution of anchors and force dipoles is not random but rather is a result of evolution comprising multiple steps of elastic and viscous relaxation and active remodeling featuring intricate feedbacks between mechanics and chemistry of network and adhesions. Importantly, in cells undergoing motility and actin flow, there exists a correspondence between spatial and temporal dimensions, e.g., position in the network on the front-back axis could be related to the time elapsed since the network creation at the leading edge. In this spirit, a recent study related cell length control to actin-depolymerization clock [33]. However, our current model lacks the temporal dimension altogether. It is significant that even a simple elastic model featuring essentially random organization of the contractile network and lacking dynamics reproduced experimental force-distance relationship. This result suggests that stress distribution truly depends on distance and is independent of network history. Network dynamics and remodeling might confer additional features that could be taken into account by more sophisticated models.

In summary, our analysis of traction force dynamics during keratocyte polarization suggests that traction force is a mediator of distance sensing and a trigger for protrusion-retraction switch. We find that traction forces increase with the distance from the cell center and correlate spatially and temporally with protrusion-retraction switches. Traction stress grows and reaches maximum soon after the onset of retraction, suggesting that adhesions do not immediately release but persist and transmit forces at the beginning of retraction phase. Force-distance relationship is recapitulated in a simple model of essentially random actin-myosin network, suggesting that it could be a fundamental emergent feature of such networks.

STAR★METHODS

Detailed methods are provided in the online version of this paper and include the following:

- KEY RESOURCES TABLE
- LEAD CONTACT AND MATERIALS AVAILABILITY
- EXPERIMENTAL MODEL AND SUBJECT DETAILS
  - Epidermal Keratocytes
  - Cell Culture
- METHOD DETAILS
  - Microscopy
  - Polyacrilamide Gel Preparation
  - Traction Force Microscopy
  - Cell Outlines and Switches
  - Stress, Distance and Curvature Analysis
  - Edge Velocity and Correlation Coefficient
  - Stress-Distance and Stress-Curvature Relationships
  - Actin Flow
  - Numerical Model
  - Biologically Relevant Parameters
  - Length
  - Spring constant
  - Force
  - Simulations
  - Model Parameters Table
- QUANTIFICATION AND STATISTICAL ANALYSIS
- DATA AND CODE AVAILABILITY

SUPPLEMENTAL INFORMATION

Supplemental Information can be found online at https://doi.org/10.1016/j.cub.2020.02.078.

ACKNOWLEDGMENTS

The work is supported by the National Science Foundation, Switzerland, grant 31003A_169972. We are grateful to Niccolo Piancentini for his help in traction force microscopy analysis.

AUTHOR CONTRIBUTIONS

A.B., Z.M., and A.B.V. performed the experiments; Z.M., A.B., F.R., and A.B.V. analyzed the data; Z.M. developed the model; Z.M. and A.B.V. wrote the paper; and F.R. and A.B.V. supervised the research.

DECLARATION OF INTERESTS

The authors declare no competing interests.

Received: August 19, 2019
Revised: December 20, 2019
Accepted: February 25, 2020
Published: March 26, 2020

REFERENCES

1. Schwarz, U.S., and Gardel, M.L. (2012). United we stand: integrating the actin cytoskeleton and cell-matrix adhesions in cellular mechanotransduction. J. Cell Sci. *125*, 3051–3060.
2. Polacheck, W.J., and Chen, C.S. (2016). Measuring cell-generated forces: a guide to the available tools. Nat. Methods *13*, 415–423.
3. Nerger, B.A., Siedlik, M.J., and Nelson, C.M. (2017). Microfabricated tissues for investigating traction forces involved in cell migration and tissue morphogenesis. Cell. Mol. Life Sci. *74*, 1819–1834.
4. Aratyn-Schaus, Y., and Gardel, M.L. (2010). Transient frictional slip between integrin and the ECM in focal adhesions under myosin II tension. Curr. Biol. *20*, 1145–1153.
5. Rape, A.D., Guo, W.H., and Wang, Y.L. (2011). The regulation of traction force in relation to cell shape and focal adhesions. Biomaterials *32*, 2043–2051.
6. Oakes, P.W., Banerjee, S., Marchetti, M.C., and Gardel, M.L. (2014). Geometry regulates traction stresses in adherent cells. Biophys. J. *107*, 825–833.
7. Murrell, M., Oakes, P.W., Lenz, M., and Gardel, M.L. (2015). Forcing cells into shape: the mechanics of actomyosin contractility. Nat. Rev. Mol. Cell Biol. *16*, 486–498.
8. Kassianidou, E., Brand, C.A., Schwarz, U.S., and Kumar, S. (2017). Geometry and network connectivity govern the mechanics of stress fibers. Proc. Natl. Acad. Sci. USA *114*, 2622–2627.

9. Wu, Z., Plotnikov, S.V., Moalim, A.Y., Waterman, C.M., and Liu, J. (2017). Two distinct actin networks mediate traction oscillations to confer focal adhesion mechanosensing. Biophys. J. *112*, 780–794.
10. Vianay, B., Senger, F., Alamos, S., Anjur-Dietrich, M., Bearce, E., Cheeseman, B., Lee, L., and Théry, M. (2018). Variation in traction forces during cell cycle progression. Biol. Cell *110*, 91–96.
11. Doyle, A., Marganski, W., and Lee, J. (2004). Calcium transients induce spatially coordinated increases in traction force during the movement of fish keratocytes. J. Cell Sci. *117*, 2203–2214.
12. Lombardi, M.L., Knecht, D.A., Dembo, M., and Lee, J. (2007). Traction force microscopy in Dictyostelium reveals distinct roles for myosin II motor and actin-crosslinking activity in polarized cell movement. J. Cell Sci. *120*, 1624–1634.
13. Ji, L., Lim, J., and Danuser, G. (2008). Fluctuations of intracellular forces during cell protrusion. Nat. Cell Biol. *10*, 1393–1400.
14. Tanimoto, H., and Sano, M. (2014). A simple force-motion relation for migrating cells revealed by multipole analysis of traction stress. Biophys. J. *106*, 16–25.
15. Barnhart, E., Lee, K.C., Allen, G.M., Theriot, J.A., and Mogilner, A. (2015). Balance between cell-substrate adhesion and myosin contraction determines the frequency of motility initiation in fish keratocytes. Proc. Natl. Acad. Sci. USA *112*, 5045–5050.
16. Raynaud, F., Ambühl, M.E., Gabella, C., Bornert, A., Sbalzarini, I.F., Meister, J.-J., and Verkhovsky, A.B. (2016). Minimal model for spontaneous cell polarization and edge activity in oscillating, rotating and migrating cells. Nat. Phys. *12*, 367–373.
17. Keren, K., Pincus, Z., Allen, G.M., Barnhart, E.L., Marriott, G., Mogilner, A., and Theriot, J.A. (2008). Mechanism of shape determination in motile cells. Nature *453*, 475–480.
18. Barnhart, E.L., Lee, K.C., Keren, K., Mogilner, A., and Theriot, J.A. (2011). An adhesion-dependent switch between mechanisms that determine motile cell shape. PLoS Biol. *9*, e1001059.
19. Guetta-Terrier, C., Monzo, P., Zhu, J., Long, H., Venkatraman, L., Zhou, Y., Wang, P., Chew, S.Y., Mogilner, A., Ladoux, B., and Gauthier, N.C. (2015). Protrusive waves guide 3D cell migration along nanofibers. J. Cell Biol. *211*, 683–701.
20. Yip, A.K., Iwasaki, K., Ursekar, C., Machiyama, H., Saxena, M., Chen, H., Harada, I., Chiam, K.H., and Sawada, Y. (2013). Cellular response to substrate rigidity is governed by either stress or strain. Biophys. J. *104*, 19–29.
21. Panzetta, V., Fusco, S., and Netti, P.A. (2019). Cell mechanosensing is regulated by substrate strain energy rather than stiffness. Proc. Natl. Acad. Sci. USA *116*, 22004–22013.
22. Giannone, G., Dubin-Thaler, B.J., Döbereiner, H.G., Kieffer, N., Bresnick, A.R., and Sheetz, M.P. (2004). Periodic lamellipodial contractions correlate with rearward actin waves. Cell *116*, 431–443.
23. Burnette, D.T., Manley, S., Sengupta, P., Sougrat, R., Davidson, M.W., Kachar, B., and Lippincott-Schwartz, J. (2011). A role for actin arcs in the leading-edge advance of migrating cells. Nat. Cell Biol. *13*, 371–381.
24. Monzo, P., Chong, Y.K., Guetta-Terrier, C., Krishnasamy, A., Sathe, S.R., Yim, E.K.F., Ng, W.H., Ang, B.T., Tang, C., Ladoux, B., et al. (2016). Mechanical confinement triggers glioma linear migration dependent on formin FHOD3. Mol. Biol. Cell *27*, 1246–1261.
25. Oliver, T., Dembo, M., and Jacobson, K. (1999). Separation of propulsive and adhesive traction stresses in locomoting keratocytes. J. Cell Biol. *145*, 589–604.
26. Fournier, M.F., Sauser, R., Ambrosi, D., Meister, J.J., and Verkhovsky, A.B. (2010). Force transmission in migrating cells. J. Cell Biol. *188*, 287–297.
27. Cai, Y., Rossier, O., Gauthier, N.C., Biais, N., Fardin, M.A., Zhang, X., Miller, L.W., Ladoux, B., Cornish, V.W., and Sheetz, M.P. (2010). Cytoskeletal coherence requires myosin-IIA contractility. J. Cell Sci. *123*, 413–423.
28. Kabaso, D., Shlomovitz, R., Schloen, K., Stradal, T., and Gov, N.S. (2011). Theoretical model for cellular shapes driven by protrusive and adhesive forces. PLoS Comput. Biol. *7*, e1001127.
29. Bangasser, B.L., Rosenfeld, S.S., and Odde, D.J. (2013). Determinants of maximal force transmission in a motor-clutch model of cell traction in a compliant microenvironment. Biophys. J. *105*, 581–592.
30. Lee, J., and Jacobson, K. (1997). The composition and dynamics of cell-substratum adhesions in locomoting fish keratocytes. J. Cell Sci. *110*, 2833–2844.
31. Anderson, K.I., and Cross, R. (2000). Contact dynamics during keratocyte motility. Curr. Biol. *10*, 253–260.
32. Begemann, I., Saha, T., Lamparter, L., Rathmann, I., Grill, D., Golbach, L., Rasch, C., Keller, U., Trappmann, B., Matis, M., et al. (2019). Mechanochemical self-organization determines search pattern in migratory cells. Nat. Phys. *15*, 848–857.
33. Ofer, N., Mogilner, A., and Keren, K. (2011). Actin disassembly clock determines shape and speed of lamellipodial fragments. Proc. Natl. Acad. Sci. USA *108*, 20394–20399.
34. Yam, P.T., Wilson, C.A., Ji, L., Hebert, B., Barnhart, E.L., Dye, N.A., Wiseman, P.W., Danuser, G., and Theriot, J.A. (2007). Actin-myosin network reorganization breaks symmetry at the cell rear to spontaneously initiate polarized cell motility. J. Cell Biol. *178*, 1207–1221.
35. Ronceray, P., Broedersz, C.P., and Lenz, M. (2016). Fiber networks amplify active stress. Proc. Natl. Acad. Sci. USA *113*, 2827–2832.
36. Tse, J.R., and Engler, A.J. (2010). Preparation of hydrogel substrates with tunable mechanical properties. Curr. Protoc. Cell Biol. *Chapter 10*, Unit 10.16.
37. JPIV. (2020). JPIV. https://www.jpiv.vennemann-online.de/.
38. Galassi, M., Davies, J.J.T., Gough, B., Jungman, G., Alken, P., Booth, M., Rossi, F., and Ulerich, R. (2019). GNU Scientific Library Reference Manual, Third Edition (Network Theory).
39. Virtanen, P., Gommers, R., Oliphant, T.E., Haberland, M., Reddy, T., Cournapeau, D., Burovski, E., Peterson, P., Weckesser, W., Bright, J., et al.; SciPy 1.0 Contributors. (2020). SciPy 1.0: fundamental algorithms for scientific computing in Python. Nature Methods *17*, 261–272.
40. Pedregosa, F., Varoquaux, G., Gramfort, A., Michel, V., Thirion, B., Grisel, O., Blondel, M., Prettenhofer, P., Weiss, R., Dubourg, V., et al. (2011). Scikit-learn: machine learning in Python. J. Mach. Learn. Res. *12*, 2825–2830.
41. Ambühl, M.E., Brepsant, C., Meister, J.J., Verkhovsky, A.B., and Sbalzarini, I.F. (2012). High-resolution cell outline segmentation and tracking from phase-contrast microscopy images. J. Microsc. *245*, 161–170.
42. Schaub, S., Bohnet, S., Laurent, V.M., Meister, J.J., and Verkhovsky, A.B. (2007). Comparative maps of motion and assembly of filamentous actin and myosin II in migrating cells. Mol. Biol. Cell *18*, 3723–3732.
43. Gabella, C., Bertseva, E., Bottier, C., Piacentini, N., Bornert, A., Jeney, S., Forró, L., Sbalzarini, I.F., Meister, J.J., and Verkhovsky, A.B. (2014). Contact angle at the leading edge controls cell protrusion rate. Curr. Biol. *24*, 1126–1132.
44. Sabass, B., Gardel, M.L., Waterman, C.M., and Schwarz, U.S. (2008). High resolution traction force microscopy based on experimental and computational advances. Biophys. J. *94*, 207–220.
45. Tseng, Q., Duchemin-Pelletier, E., Deshiere, A., Balland, M., Guillou, H., Filhol, O., and Théry, M. (2012). Spatial organization of the extracellular matrix regulates cell-cell junction positioning. Proc. Natl. Acad. Sci. USA *109*, 1506–1511.
46. Plotnikov, S.V., Sabass, B., Schwarz, U.S., and Waterman, C.M. (2014). High-resolution traction force microscopy. Methods Cell Biol. *123*, 367–394.
47. Schwarz, U.S., and Soiné, J.R.D. (2015). Traction force microscopy on soft elastic substrates: A guide to recent computational advances. Biochim. Biophys. Acta *1853* (11 Pt B), 3095–3104.
48. Broedersz, C.P., and MacKintosh, F.C. (2014). Modeling semiflexible polymer networks. Rev. Mod. Phys. *86*, 995–1036.

STAR★METHODS

KEY RESOURCES TABLE

REAGENT or RESOURCE	SOURCE	IDENTIFIER
Experimental Models: Organisms/Strains		
Black Tetra *(Gymnocorymbus ternetzi)*	Local aquarium store	N/A
Software and Algorithms		
MATLAB	https://www.mathworks.com	MATLAB
ImageJ 2	https://www.imagej.nih.gov	Fiji
FTTC plugin for ImageJ	[36]	https://sites.google.com/site/qingzongtseng/tfm
VisiView Software	Visitron Systems	N/A
JPIV	[37]	https://www.jpiv.vennemann-online.de/index.html
Gnu Scientific Library	[38]	https://www.gnu.org/software/gsl/
scipy.stats.spearmanr and scipy.stats.kstest	[39]	https://www.scipy.org/
Model implementation	This paper	https://github.com/zenomessi/lattice
sklearn.cluster.MeanShift	[40]	https://scikit-learn.org/
Chemicals, Peptides, and Recombinant Proteins		
Dulbecco's modified Eagle's medium (DMEM)	Sigma-Aldrich	Cat#D1152
Fetal Bovine Serum (FBS)	HyClone	Cat#SH30088
Amphotericin B	Thermo Fisher	Cat#15290018
Gentamicin	Thermo Fisher	Cat#15750060
Penicillin-streptomycin	Thermo Fisher	Cat#15140122
EthyleneDiamineteTetraAcetic Acid (EDTA)	Sigma-Aldrich	Cat#E9884
Trypsin-EDTA	Sigma-Aldrich	Cat#T4049
SurfaSil Silconizing Fluid	PIERCE	Cat#42800
3-Aminopropyltrimethoxysilane (3-APTMS)	Sigma-Aldrich	Cat#281778
glutaraldehyde	Sigma-Aldrich	Cat#G5882
FluoSpheres	Invitrogen	Cat#F8810
Acrylamide	AppliChem	Cat#A1089
Bis-acrylamide	AppliChem	Cat# A4989
TEMED	AppliChem	Cat#A1148
Ammonium Persulfate (APS)	Sigma-Aldrich	Cat#A3678
Sulfo-SANPAH	Thermo Scientific	Cat#22589
Fibronectin	Sigma Aldrich	Cat#F0895
(-)-Blebbistatin	Sigma-Aldrich	Cat#B0560
Cytochalasin D	Sigma-Aldrich	Cat#C8273
Calyculin A	Sigma-Aldrich	Cat#C5552
Alexa-Phalloidin	Molecular Probes	Cat#A12379
Other		
Coverslips	Menzel-Gläser	N/A
Eclipse Ti Microscope	Nikon	Model TI-DH
ORCA-flash 4.0	Hamamatsu	Cat#C11440-42U
PhotoFluor	89 North Incorporation	Cat#CT-3676

LEAD CONTACT AND MATERIALS AVAILABILITY

Further information and requests for resources and reagents should be directed to and will be fulfilled by the Lead Contact, Zeno Messi (zeno.messi@epfl.ch). This study did not generate new unique reagents.

EXPERIMENTAL MODEL AND SUBJECT DETAILS

Epidermal Keratocytes

Epidermal keratocytes from healthy Black tetra (*Gymnocorymbus ternezi*) were used for this study. Fishes were from 3 months to 2 years old. Both sexes were used indifferently. Fishes were bought at the local aquarium shop. They were kept in a fish tank in the lab. Work with fishes was performed according to the protocol approved in animal work license number 2505 from the Swiss Veterinary Office.

Cell Culture

Epidermal keratocytes from Black tetra (Gymnocorymbus ternezi) scales were cultured and imaged as described in [16, 41, 42]. First, the scales were pulled from the fish with tweezers and placed external side up on coverslip. To make sure the cells adhere to the coverslips, culture medium was added only after 30 to 60*s*. Dulbecco's modified Eagle's medium (HEPES modification) with 20% of fetal bovine serum (FBS, HyClone Laboratories Inc, San Angelo, TX, USA) supplemented with amphoterecin B ($250\mu g/ml$), penicillin ($100units/ml$) and streptomycin ($100units/ml$), and gentamicin ($100\mu g/ml$, all from ThermoFisher, Waltham, MA, USA) was used. Cells were then incubated overnight at 30° to allow them to migrate away from the scales. Next, keratocytes were detached from their neighbors and rendered isotropic by treatment with 2.5*mM* EthyleneDiamineteTetraacetic Acid (EDTA) in phosphate-buffered saline (PBS). Cells were then replenished with fresh culture medium to allow for polarization.

METHOD DETAILS

Microscopy

Phase contrast, epifluorescence and interference reflection microscopy was performed using a Nikon Eclipse Ti inverted microscope (Nikon Corporation, Minato, JP) equipped with an ORCA-flash 4.0 (Hamamatsu Photonics K. K., Hamamatsu City, JP) operated with VisiView software (Visitron Systems GmbH, Puchheim, GE). Fluorescent images were acquired using PhotoFluor (89 North Inc., Williston, VT, USA) as a light source.

Polyacrilamide Gel Preparation

For traction force microscopy, cells were plated on polyacrylamide gels with fluorescent beads following a protocol adapted from [36, 43]. The gel was made of two layers to allow the observation of the fluorescent beads without bright background.

2 18*mm* diameter (capping) coverslip and 1 25*mm* (supporting) coverslip were used for the gel preparation. First, support coverslip was treated with 0.1*N NaOH* for 5*min* and functionalized with Silane (APTMS, 97% Sigma-Aldrich) for 3*min*. It was then rinsed and placed at 37° for 10*min* for drying and let to cool at room temperature. Finally, the coverslip was treated with 0.5 volume percent glutaraldehyde (Sigma-Aldrich) for 20*min*, thoroughly rinsed with water and dried at room temperature. Functionalized coverslips could be kept for several days inside a vacuum desiccator.

Capping coverslips were hydrophobically treated with SurfaSil (SurfaSil Silconizing Fluid, PIERCE, Dallas, TX, USA). They were put in a Petri dish covered with Parafilm and $200\mu l$ of 10% by volume SurfaSil in chloroform was pipetted onto the Parafilm next to the coverslips. Subsequently the dish was placed in a vacuum dessicator for 10*min*.

For the gel, a working solution of Acrylamide (AppliChem GmbH, Darmstadt, GE), Bis-acrylamide (Applichem) and double-distilled water was prepared. Proportions could be changed to create substrates with different rigidities according to [36]. For polymerization, $200\mu l$ of working solution, $290\mu l$ of double-distilled water, $0.75\mu l$ of TEMED (AppliChem), $2.5\mu l$ of 10% ammonium persulfate (APS, Sigma-Aldrich) were mixed in a tube. $7.5\mu l$ of beads (FluoSpheres, Invitrogen, Carlsbad, CA, USA) were added to the solution for the second layer. $8\mu l$ of the solution without beads were pipetted onto the support coverslip and a capping coverslip was put on top. The gel was left to polymerize between the two coverslips for 10*min* at room temperature. Then, the capping coverslip was peeled off and the procedure was repeated with $5\mu l$ of the solution with beads and the second capping coverslip. After polymerization of the second layer, the coated coverslip was immersed in phosphate buffered saline (PBS) for at least 5*min*.

Finally, fibronectin was crosslinked to the gel with Sulfo-SANPAH. After removing the PBS from the gel coated coverslip, $200\mu l$ of $0.2mg/ml$ Sulfo-SANPAH in double-distilled water was pipetted onto the gel. The coverslip was placed under a UV-light source at a distance of $7-8cm$ for 10*min* for activation. Next, the coverslip was washed with PBS. $200\mu l$ of $10\mu g/l$ fibronectin in PBS was pipetted onto the gel and incubated overnight at 4°. The coverslip was washed one last time before transferring the scale.

Traction Force Microscopy

Traction stress was reconstructed from fluorescence image sequences with an ImageJ macro using Fourier transform traction cytometry (FTTC) method [44] implemented as a plugin, as described in [45]. The ImageJ macro is available on the github repository dedicated to this article https://github.com/zenomessi/lattice.git.

To compare stresses under various experimental conditions that differ significantly in the range of substrate deformation, it was necessary to determine the regularization parameter for FTTC method separately for each condition [44, 46, 47]. We used signal to noise ratio of the TFM image as a criterion to select optimal regularization parameter. The latter was defined as the ratio between the maximal value recorded inside the cell and the maximal value outside. The mean signal to noise ratio was computed for each experiment for a range of regularization parameters $\lambda \in [10^{-11}, 10^{-7}]$ with an increment of $10^{0.1}$. The regularization parameters giving

the highest signal to noise ratio were averaged and this value was used as the regularization parameter for the particular experimental condition. Some experiments didn't display a clear maximum but rather a plateau value toward the small values of λ. Those experiments were not taken into account. The value of the parameter for different conditions were as follows: 1.67*k Pa*: $\lambda_{1.67} = 10^{-8.9}$, 4.5*k Pa*: $\lambda_{4.5} = 10^{-9.0}$, 16.7*k Pa*: $\lambda_{16.7} = 10^{-9.5}$, blebbistatin on 16.7*k Pa*: $\lambda_{blebb} = 10^{-9.4}$, cytochalasin-D on 16.7*k Pa*: $\lambda_{cytoD} = 10^{-9.0}$ and calyculin-A on 16.7*k Pa*: $\lambda_{calyA} = 10^{-9.0}$.

Cell Outlines and Switches

Cell outlines were extracted manually from phase-contrast micrographs in ImageJ and exported in MATLAB. Each outline was digitized as a polygon with 600 vertices.

The switches from protrusion to retraction are defined as in [16]. Briefly, a protrusion-retraction switch is a region of the plane that is inside the cell at frame n but neither at frame $n-1$, nor $n+1$.

Stress, Distance and Curvature Analysis

The raw output of the FTTC algorithm is a 2048 by 2048 pixel image where the pixel value is the magnitude of the stress in Pascals. For stress-distance measurements, a grid of 16 *px*×16 *px* (i.e., 1.032×1.032 μm) squares was used. The stress was averaged in each box and the center of the box was used to measure the distance to the geometrical center of the cell defined as in [16]. In very few cases when the cells had highly crescent shapes, geometrical center was a point just outside the cell margin. These points were used for measurements in the same way as the rest of the center points (the majority) localized within the cell. As these outside center points were very few and were very close to the cell margin, repositioning them inside would not have significantly changed the results. For other measures (stress-curvature relationship, correlation coefficient, comparison with edge velocity) stress was averaged in elongated rectangles of 20 *px*×200 *px* (i.e., 1.29×12.9μm). The long axis of the rectangles was oriented normally to the local edge and centered on a point of the cell outline.

For stress profiles, points on the cell outline constantly protruding for 1*min* before the onset of retraction and constantly retracting for 1*min* after the onset of retraction were selected and analyzed. The profiles were taken on the line connecting the outline point at the onset of retraction (first time point with negative speed) to the center of the cell. A sequence of stress profiles on this line was then taken from $t = t_s - 60\ s$ to $t = t_s + 60\ s$, $t = t_s$ being the time of onset of retraction.

Local curvature was measured on portions of the cell edge representing $(1/30)$ to $(1/60)$ of the total perimeter. In stress-curvature measurements, the center of the edge portion matched the center of the rectangle where stress was averaged.

To define the centers of the force clusters, clustering of traction force microscopy data was carried out with the mean shift clustering algorithm implementation from python scikit-learn library [40]. The mean distance to the closest cluster was then measured for each point on the cell outline and each PR switching point. Finally, a Kolmogorov-Smirnov test was performed to compare the distributions of the distances, this was done with the implementation from python scipy library [39].

Edge Velocity and Correlation Coefficient

Edge velocity was measured as follows. Let $\vec{x}(t)$ be the position of a point on the cell outline at time t. Let $\vec{x}(t+\delta t)$ be the intersection of the normal to the edge through point $\vec{x}(t)$ and the cell outline at time $t+\delta t$. The velocity is defined as $\vec{v}(t) = (\vec{x}(t+\delta t) - \vec{x}(t))/\delta t$. The time intervals δt for measuring velocity were time intervals between the frames in image sequences, e.g., 10 *s* for traction force assays and 5 *s* for retrograde flow assays.

The correlation function compares locally the displacement of the edge to the variation of the stress. The interrogation window for the stress was an elongated rectangle centered on a point of the cell outline (see above). Stress variation $\Delta\sigma$ was defined as the difference in average stress in the window for two consecutive frames. To compute the correlation function, we computed the product of the local variation of the stress at time t and the local variation of the edge position Δx (i.e., edge velocity) at time $t + \Delta t$ and divided it by its absolute value. This was done for all stress-velocity pairs and the results were summed and normalized by the number of events. The correlation function,

$$C(\Delta t) = \frac{1}{N_{pairs}} \sum_{pairs} \frac{\Delta\sigma(t) \cdot \Delta x(t+\Delta t)}{|\Delta\sigma(t) \cdot \Delta x(t+\Delta t)|} \quad (1)$$

where N_{pairs} is the number of stress-position pairs. We analyzed 59900 stress-position pairs.

Stress-Distance and Stress-Curvature Relationships

Correlation in stress-distance and stress-curvature relationships was assessed using Spearman's rank correlation coefficient from python scipy implementation [39].

Actin Flow

Actin flow was imaged in polarizing cells injected with with Alexa-568 Phalloidin (A-11011, Molecular Probes) and tracked using JPIV software [37]. The time interval between frames for these experiments was 5 *s*.

Numerical Model

The model consists of a hexagonal lattice of bendable elastic bonds, local attractive dipoles and fixed anchors that represent actin filaments, molecular motors and cell-substrate adhesions, respectively. It was derived from models described in [35] and [48]. Each bond can be stretched, or be compressed and bend. To simplify the calculation of the bending energy, it is assumed that bending of each bond occurs at the midpoint between two lattice points. There are thus two types of vertices, lattice point and mid-point. Only lattice points can form dipoles and be fixed points. The model was implemented in a C++ program and the data was analyzed with C++ and python programs. The elongation and compression part of the energy is

$$E_s(\ell) = \mu \frac{(\ell - \ell_0)^2}{2}. \tag{2}$$

In this equation ℓ is the segment length and μ is a spring constant, a parameter of the model and ℓ_0 the segments rest length. We set $\ell_0 = 1.0$. Assuming the segments uniformly bend, the bending part reads

$$E_b(\theta) = 2\sin^2\frac{\theta}{2} \tag{3}$$

with θ the angular deflection between two consecutive segments (or hinges). There is no tunable bending coefficient. The bending coefficient is used as a reference for defining biologically relevant values for the parameters of the model. We also set $\mu \gg 1$ making thus the filaments almost inextensible. The full Hamiltonian reads

$$\mathcal{H} = \sum_{edges} \mu \frac{(\ell_{ij} - 1)^2}{2} + \sum_{hinges} 2\sin^2\frac{\theta_{ijk}}{2} + \sum_{dipoles} E_{d,i} \tag{4}$$

where ℓ_{ij} is the length of edge linking the vertices i and j (a lattice point and a mid-point), while θ_{ijk} is the angle formed by the two consecutive segments with vertices i, j and k (lattice-mid-lattice or mid-lattice-mid). Only segments that are aligned in the initial configuration of the network are considered to be hinges. $E_{d,i}$ is the dipole energy of dipole i. It comes from the integration of the dipole force. For numerical stability, we chose to set a continuous cut-off on the force at short distances. The force acting on a vertex of a dipole reads

$$F_d(\ell) = \begin{cases} M & if\, \ell > \ell_c \\ M\left(\frac{2\ell}{\ell_c} - 1\right) & if\, \frac{\ell_c}{2} < \ell < \ell_c \\ 0 & if\, \ell < \frac{\ell_c}{2} \end{cases} \tag{5}$$

where M is the tunable parameter for the magnitude of the force, ℓ is the distance between the vertices of the dipole and ℓ_c is a cut-off length introduced for numerical stability. It is set to $\ell_c = \ell_0/10^4$. Thus the dipole energy is

$$E_d(\ell) = \begin{cases} M(\ell - \ell_c) + \frac{M\ell_c}{4} & if\, \ell > \ell_c \\ \frac{M}{\ell_c}\ell^2 - M\ell + \frac{M\ell_c}{4} & if\, \frac{\ell_c}{2} < \ell < \ell_c \\ 0 & if l < \frac{\ell_c}{2} \end{cases} \tag{6}$$

The other parameters of the model are the densities of bonds ρ, of dipoles ρ_d and the anchor density ρ_a. The first two are defined as the probability that two neighboring lattice points are linked by an elastic bond, respectively a dipole. The anchor density is defined as the probability for a lattice vertex to be a fixed point. Table S1 lists the model parameters.

Biologically Relevant Parameters

As the model is dimensionless, it is essential to give orders of magnitude for its parameters.

Length

The distance between crosslinks in a cell cytoskeleton lies in the range $\xi \sim 0.1 - 1.0\mu m$. This distance can be identified to the size of the mesh (distance between two lattice points) in the model $\ell_0 = (\xi/2) = 1.0$ thus a unit of length in the model represents $0.05\mu m$ to $0.5\mu m$ in reality.

Spring constant

Following [35], we use a Worm-Like Chain (WLC) model to describe the actin filaments. In this framework, one can compute a ratio between the spring constant and the bending coefficient in terms of the mesh size and the persistence length. Since the bending coefficient is set to 1, the ratio defines the stretching coefficient

$$\mu = \frac{45\ell_p}{2\xi} \tag{7}$$

The typical persistence length for an actin fiber is $\ell_p \sim 10\mu m$. Thus the range for the spring constant in the model is

$$\mu \sim 200 - 2000. \tag{8}$$

Force

Actin filaments can be modeled as thin elastic beams. Under a sufficient compressive longitudinal stress, beams will buckle. The critical force to apply to the beam is Euler force defined as

$$F_{cr} = \frac{\pi^2 kT\ell_p}{\xi^2} \tag{9}$$

Under this threshold, the filament doesn't buckle. Experimentally the force that is necessary to bow a filament is in the range $F_b \sim 0.4 - 40pN$. The magnitude of the force in the model is in units of the buckling force. Conversely, a myosin II motor power stroke is of the order of magnitude of $4pN$. In units of the buckling force, this yields for the magnitude of the force

$$M \sim 0.1 - 10. \tag{10}$$

Simulations

A new random lattice was initialized with a homogeneous random distribution of bonds, dipoles, and anchors. Then the system was left to find an energy minimum through an iterative optimization algorithm. BFGS implementation from the GNU Scientific Library was used [38]. Once a minimum was reached, the final configuration was saved and could be analyzed. This procedure was carried out for a large variety of biologically relevant values of the parameters and for many initial outlines. A sketch of the model is shown in Figure 4A with an example of a typical initial and final state.

Model Parameters Table

A table recapitulating the model parameters and the ranges in which they were used in this paper is given in Table S1.

QUANTIFICATION AND STATISTICAL ANALYSIS

Spearman's rank correlation coefficient implementation from python scipy was used to assess the correlation between the stress exerted by cells and geometrical observables i.e., local edge curvature and center to edge distance in Figures 2A, 2B, and 4E. Kolmogorov-Smirnov test was used to the two distributions of Figure S1.

DATA AND CODE AVAILABILITY

The C++ implementation of the model is available publicly at https://github.com/zenomessi/lattice.git